Journal of The Electrochemical Society

OPEN ACCESS

The Operation Window of Lithium Iron Phosphate/Graphite Cells Affects their Lifetime

To cite this article: Eniko S. Zsoldos *et al* 2024 *J. Electrochem. Soc.* **171** 080527

Journal of The Electrochemical Society, 2024 **171** 080527

The Operation Window of Lithium Iron Phosphate/Graphite Cells Affects their Lifetime

Eniko S. Zsoldos,[1] Daphne T. Thompson,[1] William Black,[1] Saad M. Azam,[1] and J. R. Dahn[1,2,*,z]

[1]*Department of Chemistry, Dalhousie University, Halifax B3H 4R2, Canada*
[2]*Department of Physics and Atmospheric Science, Dalhousie University, Halifax B3H 4R2, Canada*

Lithium iron phosphate (LFP) battery cells are ubiquitous in electric vehicles and stationary energy storage because they are cheap and have a long lifetime. This work compares LFP/graphite pouch cells undergoing charge-discharge cycles over five state of charge (SOC) windows (0%–25%, 0%–60%, 0%–80%, 0%–100%, and 75%–100%). Cycling LFP cells across a lower average SOC results in less capacity fade than cycling across a higher average SOC, regardless of depth of discharge. The primary capacity fade mechanism is lithium inventory loss due to: lithiated graphite reactivity with electrolyte, which increases incrementally with SOC, and lithium alkoxide species causing iron dissolution and deposition on the negative electrode at high SOC which further accelerates lithium inventory loss. Our results show that even low voltage LFP systems (3.65 V) have a tradeoff between average SOC and lifetime. Operating LFP cells at lower average SOC can extend their lifetime substantially in both EV and grid storage applications.

 [DOI: 10.1149/1945-7111/ad6cbd]

Manuscript submitted July 4, 2024; revised manuscript received August 6, 2024. Published August 21, 2024.

Supplementary material for this article is available online

$LiFePO_4$ (LFP) is a low cost cathode material using sustainable and abundant iron compared to Ni and Co-containing NMC chemistries, making it an attractive battery material.[1–3] LFP is projected to surpass NMC chemistries in the Li-ion battery market share in 2028.[4] The global battery demand is expected to grow from 0.7 TWh in 2022 to between 2.6–6.0 TWh by 2030 according to varying estimates.[5,6] While these production growth trajectories are exciting for the battery industry to transition our global energy infrastructure to renewable energy, we must prioritize long battery lifetime to gain energy independence. Aiken et al.[5] clearly demonstrated that if battery lifetimes are too short, we will be wasting resources to replace our existing fleet of dying batteries, rather than making progress on creating new batteries that displace fossil fuels. Therefore, this work focuses on increasing LFP cell lifetime for this sustainable transition.

$LiFePO_4$ was discovered as an lithium intercalation positive electrode material by Pahdi, Nanjundaswamy and Goodenough in 1997.[6] The olivine crystal structure of LFP has poor electronic conductivity resulting in slow charge discharge kinetics and poor rate capability. LFP was improved by carbon coatings and small particle sizes in the 2000s by Ravet, Zaghib and Armand at Hydro Quebec.[7] Today, LFP cells are often considered to have long lifetime because they are low voltage cells (<3.65 V) with no passivating interphase on the cathode and minimal electrolyte oxidation.[8] LFP electrodes have a coexistence of $FePO_4$ and $LiFePO_4$ phases during operation, and this phase separation creates a flat voltage vs capacity profile as the Gibbs Free Energy is minimized.[1]

A variety of degradation modes for LFP cells have been investigated in the literature,[1] including thermal degradation, Fe dissolution, reversible storage loss, and lithium inventory loss at the negative electrodes. Safari and Delacourt[9] showed that inventory loss is the primary degradation mode and that there is no impedance growth in LFP cells. Additionally, they showed that higher temperatures cause more capacity fade in LFP cells (45 °C vs 25 °C) and cycling causes more fade than storage does for LFP. Aiken et al.[10] confirmed this failure mode and lack of impendence growth. Kassem[11] and Zheng[12] showed higher irreversible and reversible capacity losses in LFP/graphite cells at higher temperatures and higher SOCs, but found that temperature was the more important variable compared to SOC in determining capacity loss. Keil et al.[13] demonstrate that storage at high states of charge leads to more lithium inventory loss in both NMC and LFP cells, but that the LFP cells show minimal resistance increase during storage. Logan et al.[14] showed that higher electrode drying temperature is important to lower water contamination in the electrodes because it can create acidic species from $LiPF_6$ hydrolysis. Other variables found to improve cycle life were: using VC as an electrolyte additive,[14] using a medium particle size and surface area of LFP (11.2 m^2/g),[15] using artificial graphite over natural graphite,[15] and LiFSI over $LiPF_6$ electrolyte salt.[16]

Using dV/dQ analysis, Logan et al.[15] showed that lithium inventory loss, also called shift loss, is the dominant failure mode of LFP cells, whereby the positive and negative electrode potential vs. state of charge curves are shifting with respect to each other, such that the full cell capacity is reduced. The mechanism behind this shift loss is electrolyte reduction on the negative electrode surface, in a process of solid electrolyte interphase (SEI) growth, which has been modelled to grow with a square root time dependence.[17] SEI modelling work by Von Kolzenberg et al.[18] shows that SOC impacts SEI growth significantly, along with temperature and current. Their work used NMC622 and NMC111 cells, which operate at higher voltages than LFP cells, therefore some of their observed degradation at high SOC could be from the higher voltages in NMC cells (4.2 V), particularly electrolyte oxidation on the positive electrode. To ensure that SEI growth is the primary degradation mechanism, it would be beneficial to have similar studies on LFP cells modelling the effects of SOC and temperature on SEI growth.

Our research question is to understand how the average SOC affects cycling performance of LFP/graphite cells and to determine the underlying mechanisms. Knowing that the primary degradation mode in LFP cells is lithium inventory loss on the negative electrode due to SEI growth, we chose a full factorial design of experiment with 2 values for each of 4 variables: graphite (two suppliers), electrolyte salt ($LiPF_6$ vs LiFSI), temperature (40 °C vs 55 °C) and SOC range (0%–25% vs 75%–100%). We selected the variables of graphite type, temperature and electrolyte salt based on Logan's past works[14–16] showing that these variables are critical for LFP performance. With the new variable of SOC window in this study, we can measure how the sensitivity of LFP fade rates depends on

*Electrochemical Society Fellow.
[z]E-mail: jeff.dahn@dal.ca

SOC compared to their known dependence on temperature, salt, and graphite. After these initial studies, follow up experiments were made using the SOC ranges: 0%–60%, 0%–80% and 0%–100%.

Methods

Electrolyte.—The electrolyte used was a solvent blend of ethylene carbonate (EC): dimethyl carbonate (DMC) 3:7, 2 wt% vinylene carbonate (VC), 1.5 M LiFSI or $LiPF_6$. Throughout this work the electrolyte salt choice of $LiPF_6$ or LiFSI is specified in figure legends.

Cell specifications.—240 mAh nominal dry (no electrolyte) wound pouch cells manufactured by LiFUN Technologies (Zhuzhou City, Hunan Province, P.R.China) were cut open in an argon-filled glovebox, baked at 120 °C under vacuum for 14 h. The cells were filled with 0.85 ml (1.0 g) electrolyte and sealed under −90 kPa and 160 °C using an MTI Corp vacuum sealer. The two cell types used in this work were LFP/artificial graphite (AG), with identical LFP specifications and two different AG suppliers. The AG1 used in this work was previously characterized thoroughly and denoted as AGC in works by Eldesoky et al.,[19,20] while AG2 was not studied previously.

The active material and electrode specifications are listed in Table I.

Formation.—The formation condition in this study was at 40 °C, with an initial charge to 1.5 V, then a 24 h voltage hold at 1.5 V for electrolyte wetting, followed by a C/20 constant current (12 mA) charge to 3.65 V, and discharge to 2.5 V.

Voltage hold protocol.—Four LFP/AG1 cells with LiFSI were charged and held at either 3.0 V or 3.65 V at 60 °C for 1000 h. Every 100 h during the 1000 h test, these cells completed a C/3 cycle.

Cycling protocols.—A group of 32 LFP/AG cells were put onto ultra-high precision coulometry (UHPC) testing and 32 cells were put onto long term cycling on Neware chargers. These cycling tests were done across the various SOC windows using constant current and constant capacity cycling conditions, as described in Fig. 1. The UHPC tests consisted of 80 cycles at C/20 rate (12 mA) at temperatures of 40 °C and 55 °C, with coulombic efficiencies shown in Fig. S1. The Neware tests consisted of C/3 rate cycling at 40 °C and 55 °C, with C/20 checkup cycles (over the entire 0%–100% SOC range) every 200 cycles, tested for ∼1400 cycles, ∼2500 h. For easier comparison with other units of current used in the literature, our C/3 rate converts to currents and current densities of 80 mA or 1.06 mA cm^{-2} positive electrode area or 61.5 mA g^{-1} active LFP mass.

Gas measurement.—The evolved gases from pouch cells during formation and cycling were measured using the Archimedes method described by Aiken et al.[21]

Electrochemical impedance spectroscopy (EIS).—EIS spectra were measured using a BioLogic VMP3 system in a 10 °C temperature box, at 50% SOC, using 100 kHz to 10 mHz frequency ranges with 10 points per decade, and 50 mV_{pp} sinusoidal pulses.[22] The impedance measurements were normalized to the geometric active areas of the positive electrodes of the LFP cells: 71 cm^2 and 82 cm^2 for LFP/AG1 and LFP/AG2 cells respectively. The charge transfer resistance (R_{ct}) values were taken from Nyquist plots as the semicircle diameter of the real impedance component.

Electrolyte analysis.—Post cycling the pouch cells were filled with 1.0 g methyl acetate (MA) as an electrolyte extraction solvent. The cells were allowed to equilibrate for >1 month to ensure uniform mixing between the aged electrolyte in the electrode pores and the MA. From each cell, ∼0.75 g diluted electrolyte mixture was extracted, of which ∼500 μl went to NMR analysis alongside 20 μl g internal standard (IS) and 100 μl was further diluted for liquid gas chromatography mass spectroscopy (GCMS) analysis.

NMR was used quantitatively to determine LiFSI and $LiPF_6$ concentrations, as well as mass ratios of EC, DMC, VC and DMOHC in the extracted sample via an internal standard. NMR samples were prepared inside an Ar-filled glovebox with 200 MHz 5 mm diameter NMR tubes. NMR experiments were conducted using an Avance Neo 400 MHz NMR spectrometer (Bruker). Chemical shift values for ^1H NMR and ^{19}F NMR experiments were internally referenced to the internal standard 1,4-bis(trifluoromethyl)benzene at 7.88 ppm (^1H) and −63.86 ppm (^{19}F). GCMS samples were prepared in 15 ml high-clarity conical tube (FALCON). Electrolyte, 100 μl, was diluted to a total volume of 5.0 ml with dichloromethane (DCM). Using liquid-liquid extraction, non-volatile and water soluble components of the electrolyte were extracted using two rinses with 0.1 ml of distilled water. Following liquid-liquid extraction, samples were dried using anhydrous magnesium sulfate (Sigma Aldrich) and 1.5 ml of the DCM solution was transferred to GCMS vials (Agilent Technologies). GCMS was carried out using a Bruker 436 GC coupled to an Agilent 5977B single-quadrupole mass spectrometer with a 70 eV ion source. The column used was a BR-5MS (5% phenyl, 95% dimethyl arylene siloxane) 30 m column with an inner diameter of 0.25 mm and a 1 μm thick coating. The oven temperature was ramped from 30 °C to 260 °C at a rate of 15 °C min^{-1}. The flow rate of the carrier gas, He, was 0.68 ml min^{-1}.

Scanning μXRF.—Samples were prepared by discharging cells post cycle testing below 2.5 V, cutting open the pouch cells in a fume hood, separating the electrodes, and allowing them to dry for 24 h. Samples of 2 cm × 3 cm were cut from the anode and taped onto an acrylic plate. The Bruker μXRF parameters used were a Rh X-ray source, Al 200 μm Ti 200 μm filter, 600 μA tube current, 50 kV accelerating voltage, 100 μm pixel size, 15 ms/pixel scan rate, and two spectrophotometers detecting counts of 0 to 15 keV. The Fe Kα peak (6.4 keV) was integrated by the Bruker software. Calibration standards were prepared on dry graphite-coated copper

Table I. Pouch cell and electrode material specifications used in this work.

		LFP/AG1	LFP/AG2
LFP Material Specifications	BET surface area (m^2/g)	11.2	
	D50 (μm)	1.4	
	Carbon content %	1.3	
	Half Cell Capacity at room temp (mAh/g)	155	
Artificial Graphite Material specifications	Particle Size D50 (μm)	15.6	13.5
	Surface area (m^2/g)	1.0	1.7
	Tap density (g/cm^3)	1.12	1.10
Negative Electrode	Mass Loading (mg/cm^2)	8.9	9.0
	Electrode density (g/cm^3)	1.43	1.46
Positive Electrode	Mass Loading (mg/cm^2)	17.3	17.3
	Electrode density (g/cm^3)	2.43	2.44

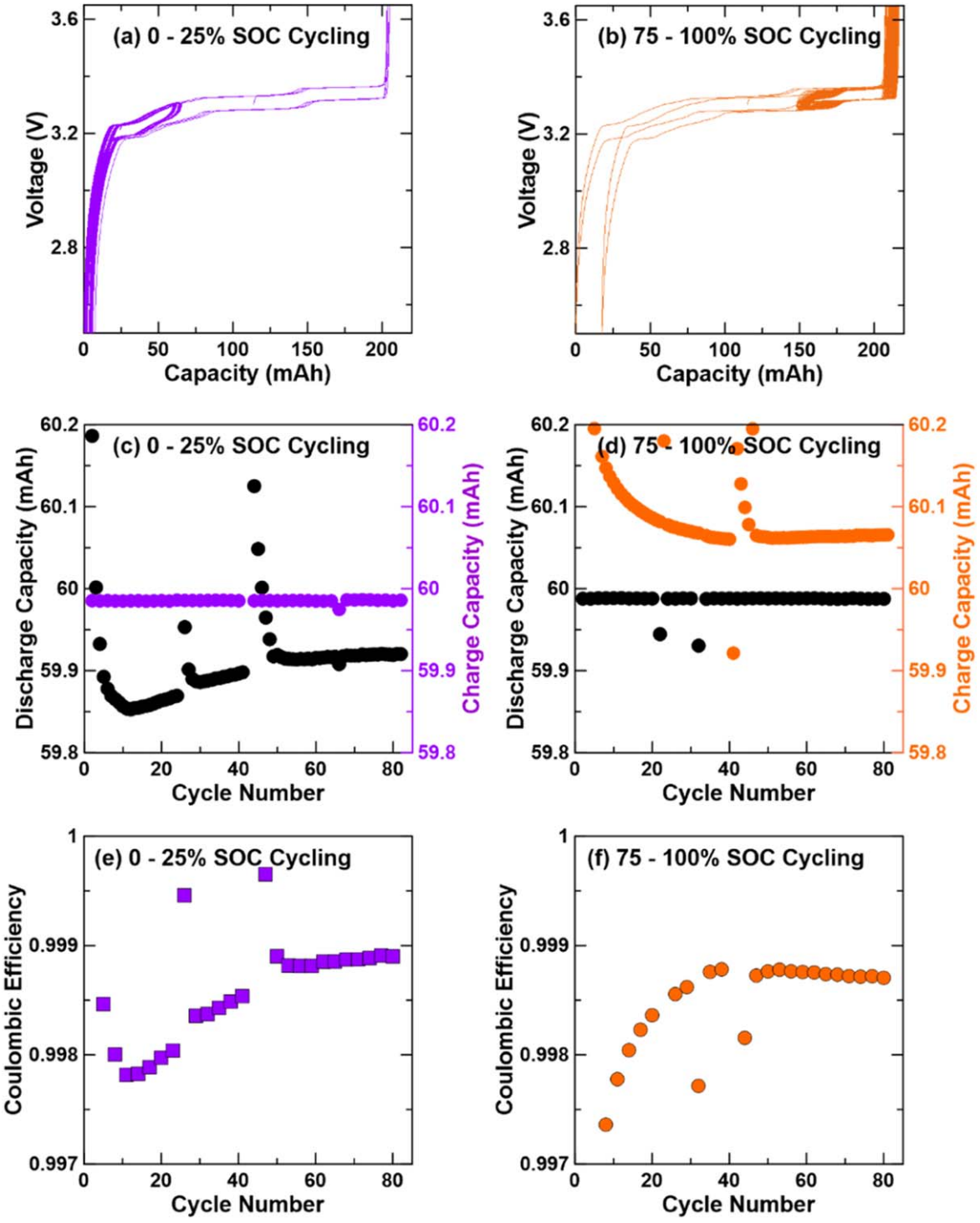

Figure 1. Cell cycling protocol for LFP/graphite pouch cells operating across two state of charge (SOC) windows, with either fixed discharge or fixed charge capacities. (a) Voltage vs capacity of LFP/graphite cells cycled between 0%–25% SOC with 60 mAh constant charge capacity and variable discharge capacity to 2.5 V lower cutoff voltage. (b) Voltage vs capacity when cycling 75%–100% SOC with constant discharge capacity of 60 mAh, and variable charge capacity to 3.65 V upper cutoff voltage. Discharge and charge cell capacities per cycle when cycling between (c) 0%–25% and (d) 75%–100% SOC. Coulombic efficiency per cycle when cycling over (e) 0%–25% SOC and (f) 75%–100% SOC. Testing is done at C/20 rate (12 mA) at 55 °C. Every 40 cycles there is a full voltage range 2.5 V–3.65 V check-up cycle (0%–100% SOC). Electrolyte is EC:DMC 3:7 2VC 1.5 M LiFSI. A power outage affected the data around cycle 27.

foil, with a gradient of sputtered Fe loading (5 to 35 μg cm^{-2}), to establish a calibration factor of 0.001047 μg/count to convert from XRF signal to a Fe mass per area, and this linear regression analysis for the calibration samples had an error of ±4.6%. This method is described in more detail here.[23] The background signal from the dry pristine graphite electrode is 1.45 μg Fe/cm^2.

Error analysis.—The statistics used are n = 2 for duplicate cells throughout this work, except in the case of causal variable fade rate analysis where n = 16 was used. The error bars shown throughout for capacity fade rates are from duplicate cells. Additionally, for the Fe deposition results, error was propagated from the XRF calibration factor and the duplicate cells. This standard error analysis is the

square root of the sum of the squared errors from the Fe calibration standards and the error from measurements on duplicate cells.

IMC method.—The isothermal microcalorimeter (IMC) instrument used is a thermally activated module (TAMIII) microcalorimeter by TA Instruments. The measured heat flow to and from each ampoule has 1 nW precision and 1 μW accuracy, and the signal to noise ratio is 100–1000:1.[24] In the pouch bag experiment, following formation and 4 initial cycles ending at specified states of charge (SOC), the pouch cells were cut open in an Ar-filled glovebox, and the electrodes were removed and separated. The lithiated graphite electrodes were then re-folded and re-sealed into new pouch bags, with 0.1 ml DMC added to compensate for the evaporated volatile electrolyte components, assuming the salt and EC remained in the pores of the graphite electrodes during disassembly. Next, the pouch bags were put into the TAMIII at 40 °C for 250 h to measure open circuit heat flow from the negative electrodes in isolation. Note that for the IMC experiment, the pouch cells are NMC532/AG cells balanced to 3.8 V, not LFP cells.

ICP method.—Electrolyte extraction for the lithium methoxide experiment was done in a liquid-liquid extraction of 2% HNO_3 (aq)

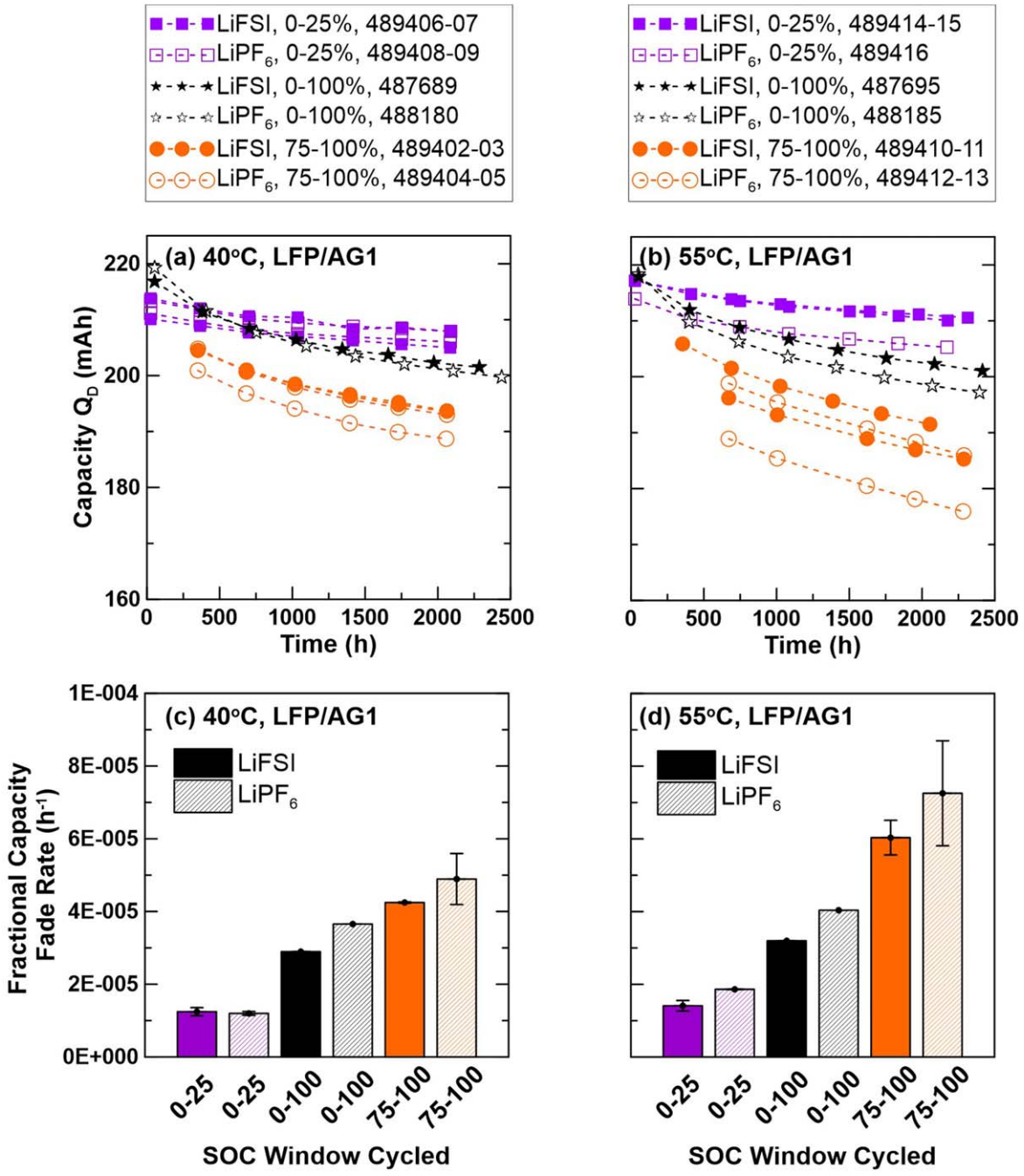

Figure 2. LFP/**AG1** cell cycling capacity fade across different SOC ranges in long-term cycling over 2500 h. All cells had identical capacity throughput. For best comparison, only the C/20 checkup cycles are plotted, where all cells cycle 0%–100% every 200 cycles or every ∼300 h. The regular cycles are at C/3 rate, and only 60 mAh are cycled for the 0%–25% and 75%–100% SOC cells. Discharge capacity vs cycling time is plotted for (a) 40 °C and (b) 55 °C testing of LFP/AG1 cells with $LiPF_6$ and LiFSI electrolyte salts at various SOC operation windows. The cell barcode IDs are indicated in the legends. The normalized discharge capacity fade per hour at (c) 40 °C and (d) 55 °C is summarized after 2500 h of cycling for the different SOC windows cycled. Electrolyte is EC:DMC 3:7 2VC 1.5 M salt.

and dichloromethane (DCM). The dissolved transition metals (Fe) and lithium salts ($LiPF_6$, LiFSI) reside in the top aqueous layer, while the organic components (DMOHC, VC, EC, DMC) are in the bottom organic layer in DCM. The approximate masses used are 0.2 g extracted electrolyte from cells, 5.0 g DCM (discarded), and 2 washes of 1.0 g 2% HNO_3. The exact mass for each sample is recorded and used to convert from Fe concentration in the ICP sample dissolved in HNO_3 to Fe concentration in the cell electrolyte. The samples of dissolved Fe in HNO_3 were analyzed using ICP-OES (iCAP 7400 Dual View, Thermo Fischer Scientific, USA) by Daniel Chevalrier at the Minerals Engineering Laboratory at Dalhousie University.

Results

Figure 1 shows the cell cycling protocol for LFP/AG cells in two operation windows: 0%–25% in Fig. 1a and 75%–100% in Fig. 1b. The protocol has full voltage range (2.5–3.65 V) check-up cycles after every 40 partial cycles. The limited window cycling in the 0%–25% SOC condition has a fixed lower cutoff voltage of 2.5 V with varying discharge capacity and a fixed charge capacity of 60 mAh, as shown in Fig. 1c. Conversely, the 75%–100% SOC cycling scenario has a fixed upper cutoff voltage of 3.65 V resulting in varying charge capacities each cycle and a fixed discharge capacity of 60 mAh, shown in Fig. 1d. The coulombic efficiencies (CE) of the

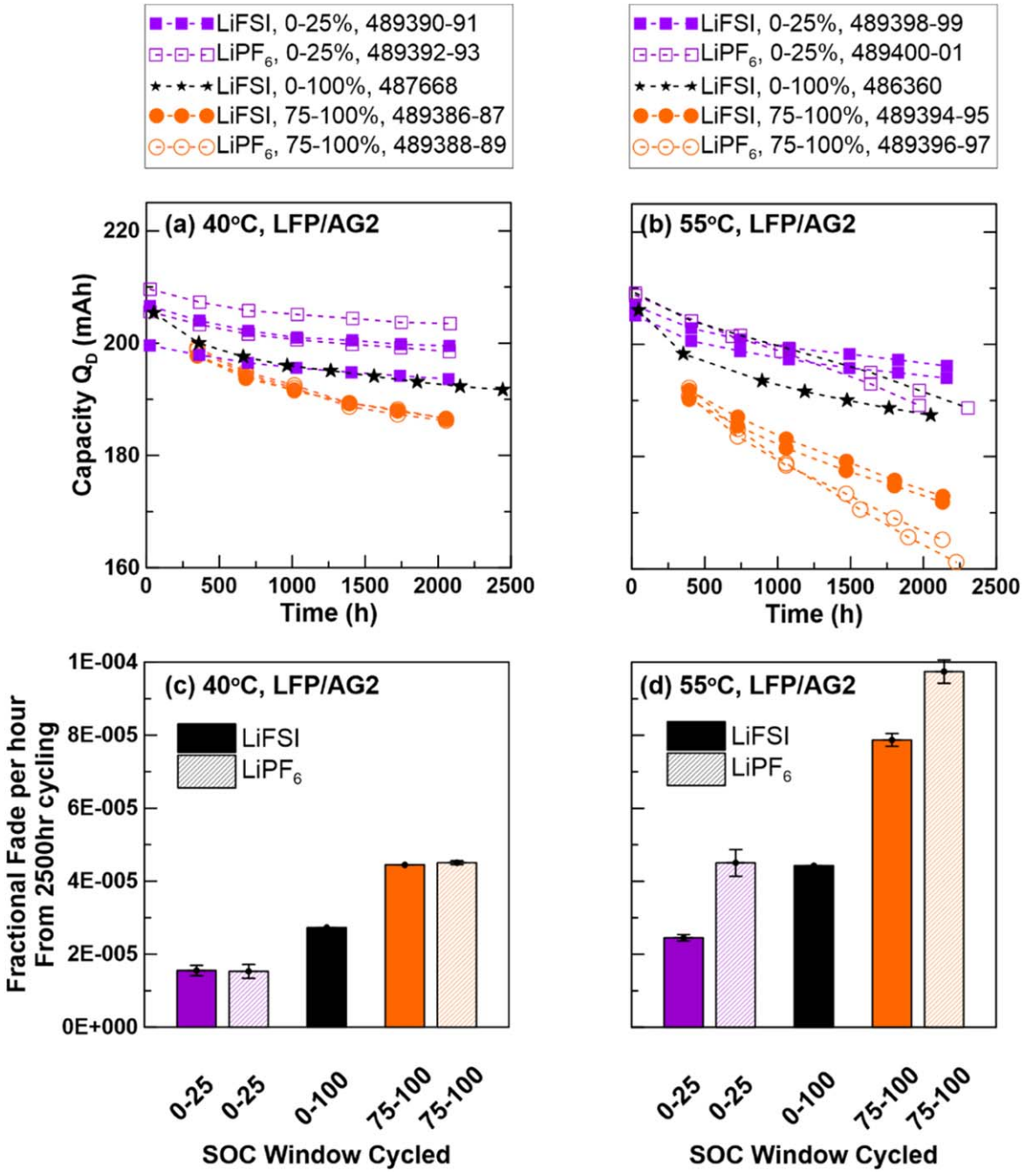

Figure 3. LFP/**AG2** cell cycling capacity fade across different SOC ranges in long term cycling over 2500 h. All cells had the same capacity throughput. For best comparison, only the C/20 checkup cycles are plotted, where all cells cycle 0%–100% every 200 cycles or every ∼300 h. The regular cycles are at C/3 rate, and only 60 mAh are cycled for the 0%–25% and 75%–100% SOC cells. Discharge capacity vs cycling time is plotted for (a) 40 °C and (b) 55 °C testing of LFP/AG2 cells with $LiPF_6$ and LiFSI electrolyte salts at various SOC operation windows. The cell barcode IDs are indicated in the legends. The normalized discharge capacity fade per hour at (c) 40 °C and (d) 55 °C is summarized after 2500 h of cycling for the different SOC windows cycled.

limited SOC window cycles are shown in Figs. 1e–1f, and this demonstrates that the CE is approaching 1.0 as the cells mature with cycling, matching the trends expected in full SOC ranges.[25] These data were collected on UHPC chargers, so we can report precise CE values of 0.99894 ± 0.00005 in the case of LFP/AG2 tested at 55 °C with LiFSI salt operating between 0%–25% SOC. We tested two temperatures (40 °C and 55 °C), two artificial graphites (AG1 and AG2), two electrolyte salts (LiFSI and $LiPF_6$) and two SOC ranges (0%–25% and 75%–100%). For these 16 test conditions each with duplicate cells, the final CE values at cycle 82 with errors are shown in Fig. S1. The process for calculating the CE values was taking an average of the last 5 cycles, where the cells have reached a steady state of CE, as seen in Figs. 1e–1f, with the errors being propagated from the standard deviation of those last 5 cycles CE values and the pair cell error. The cells cycled at 40 °C show larger CE than at 55 °C, and cells with AG1 show larger CE than AG2. The effects of salt and SOC window are unclear from these CE measurements alone. The 4 test conditions with AG2 at 55 °C show lower CE than the other 12 conditions, and we attribute this graphite's poor performance at elevated temperature to its higher surface area, having additional sites for electrolyte reduction.

Next, we performed longer term charge-discharge cycling tests on fresh LFP/AG cells using the same 16 test conditions. Figure 2 shows the results for the 8 conditions involving AG1 cells with 40 °C in Figs. 2a, 2c and 55 °C testing in Figs. 2b, 2d. In these tests, the cycling is done at a faster rate of C/3 with respect to the full cell nominal capacity, meaning 80 mA constant current charge and discharge of 60 mAh fixed capacity (25% depth of discharge windows). Slow C/20 (12 mA) check-up cycles with full SOC ranges are done every 200 cycles, roughly every 300 h. In Figs. 2a–2b, only the check-up cycle discharge capacities are plotted, so that the cell capacity fade over time can be observed. Additionally, reference cells cycling over 0%–100% SOC windows are also shown, and for best comparison only their check-up cycles are plotted. Since these different depth of discharge (DOD) conditions have different durations per cycle, the capacity fade is plotted vs time rather than vs cycle number. Figure 2 shows that the high SOC window cells fade faster, while the low SOC cells retain their capacities longer, and that the 0%–100% SOC cells are intermediate in fade. Figures 2c–2d show rates of fractional discharge capacity fade per hour and this clearly shows that the high SOC window is the most significant factor in increasing capacity fade rate. The effect of temperature and salt are as expected: 55 °C fades faster than 40 °C and the $LiPF_6$ fades faster than LiFSI particularly at the higher temperature, matching previous studies.[16] This comparison in Figs. 2c–2d shows that while temperature can affect fade rates on the order of 15%–50% and salt can affect fade rates by 5%–30%, the SOC window has the most significant effect on fade rates with 250%–400% changes. Therefore, cycling LFP/AG cells across low SOC windows appears to be the most impactful way to improve cycle life among these conditions tested.

These tests were repeated for a second artificial graphite type, LFP/AG2 cells in Fig. 3, following the same format of plots. Check-up cycle discharge capacity fades are shown in Figs. 3a–3b and the normalized fade rates are shown in Figs. 3c–3d. For these plots describing results from cells with AG2, temperature has a greater effect on fade than it did for AG1 in Fig. 2, however, the most significant variable influencing fade remains the SOC window. Comparing the graphites between Figs. 2 vs 3, AG1 in Fig. 2 performs better with a 40% lower fade rate on average in each condition. We can attribute this to the particle surface area differences between the graphites shown in Table I. Overall, the best performing combination among the 16 conditions is: lower temperature (40 °C), LiFSI electrolyte salt, low SOC window (0%–25%) and lower surface area graphite (AG1).

The designations of SOC windows (0%–25% and 75%–100%) are based on the initial nominal cell capacity of 240 mAh, cycling 60 mAh fixed capacity. However, as capacity fade occurs over lifetime, the effective SOC window changes. In the most severe case of capacity fade to 160 mAh, the effective depth of discharge of 60 mAh capacity is 37.5%, increased from 25%. Therefore, the true window of operation in the final cycle shown is 62.5%–100% rather than 75%–100%. For the cells cycling with minimal fade and a stable capacity at 210 mAh, the true window is 0%–28%, remaining close to the original SOC window.

Comparing our results to literature, there are surprisingly few studies investigating the effects of cycling LFP/graphite cells over different average SOC windows, with a fixed depth of discharge. One study by Stroe et al.[26,27] shows that cycling LFP/graphite cells over a lower average SOC leads to more capacity fade than a higher average SOC, which is the opposite of our findings. Their cells were cycled with parameters of 4 C:4 C rate, 42 °C, 35% depth of discharge. Those results are at a 12x higher C-rate than this work and could be confounded by lithium plating at fast currents. However, those same works[26,27] also show that storage at high SOC causes more capacity fade than low SOC, and this is consistent with our work and the rest of the literature.[11–13] Therefore, it is possible that there are different failure regimes in how SOC affects capacity fade; dependent on the current. More work is needed to verify the effect of high C-rates in various SOC windows.

It is clear that the average SOC of operation is critical in capacity fade, but what is the mechanism for this? After the cells completed ~2500 h of cycling, they were discharged and disassembled for XRF analysis of the negative electrodes. Photographs of some of the negative electrodes and separators are shown disassembled in Fig. S2, showing that the components from cells with LiFSI are stained slightly yellow and with varying amounts of electrode delamination. Bar charts of the Fe deposition on the negative electrode in each condition are shown in Figs. 4a–4d, and a correlation plot of capacity fade rate vs Fe deposition loading is shown in Fig. 4e. Based on these results, capacity fade correlates with Fe deposition. Figure 4e shows that the cells cycled at high SOC have higher capacity fade rates and have a weak correlation to Fe deposition. This means that cycling LFP cells over high SOC windows is detrimental through a different capacity fade mechanism, that will be discussed in Fig. 5, in addition to the iron dissolution and deposition.

The cells cycled over the low SOC window (0%–25%) have a clearer linear correlation between fade rate and iron deposition, showing that Fe deposition causing Li inventory loss is the primary degradation mode for low SOC cells. The factors that exacerbate the Fe deposition in the low SOC window are higher temperature and higher surface area graphite. We hypothesize that lithium alkoxide species that are created on the imperfectly passivated graphite surface at high temperatures lead to the Fe dissolution at the positive electrode. The Fe then deposits on the negative electrode and leads to electrolyte reduction consuming lithium inventory and leading to the observed capacity fade. This mechanism will be explored later in this paper.

A 1000 h long voltage hold experiment at 60 °C with LFP/AG1 cells was conducted and these results are shown in Fig. 4b alongside the cycled LFP/AG1 cells at 55 °C. These LFP cells held at either 0% SOC (3.0 V) or 100% SOC (3.65 V) showed no observable Fe deposition above background levels, despite these being extreme conditions of temperature, SOC and time. We conclude that the Fe dissolution and deposition mechanism in LFP is independent of SOC during storage: neither Fe^{2+} nor Fe^{3+} are likely to dissolve from the respective $LiFePO_4$ and $FePO_4$ phases during a voltage hold. Instead, the process of lithium deintercalation during charge-discharge cycling enables Fe dissolution through unit cell volume changes. Our interpretation of the calendar aging tests at 60 °C shown in literature,[9,11,28] is that storage does not accelerate degradation via iron dissolution, but rather through lithium inventory loss from SEI growth. These results corroborate the literature that cycling is more detrimental to capacity fade than storage in LFP cells,[28] and the reason is that Fe dissolution primarily occurs during cycling.

Next, we conducted an isothermal microcalorimetry (IMC) experiment to understand the mechanism for cell degradation at

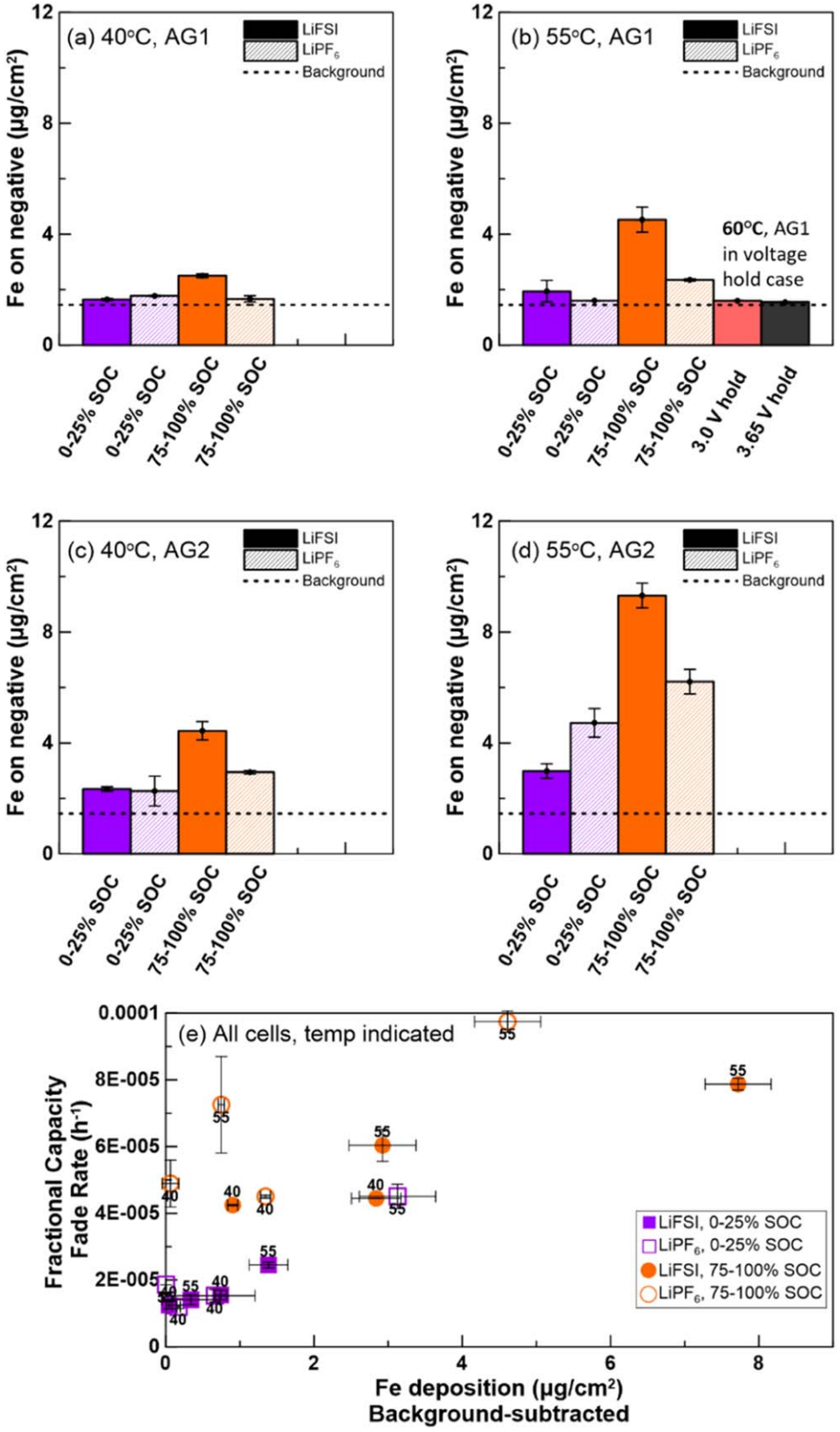

Figure 4. Iron dissolution and deposition on the negative electrodes of LFP/AG cells after cycling through various states of charge windows, as measured by XRF. (a), (b) LFP/AG1 cells at 40 °C and 55 °C. (c), (d) LFP/AG2 cells at 40 °C and 55 °C. (e) capacity fade rate correlation to Fe deposition for all cells tested.

various states of charge. In this experiment graphite was lithiated to specific states of charge to investigate its reactivity with electrolyte, independent of any transition metal dissolution, electrolyte oxidation or any other capacity fade mechanisms. We chose NMC532/AML400 cells balanced to 3.8 V and charged the cells to 6 states of charge between 0 to 100% after 4 initial cycles. These cells have

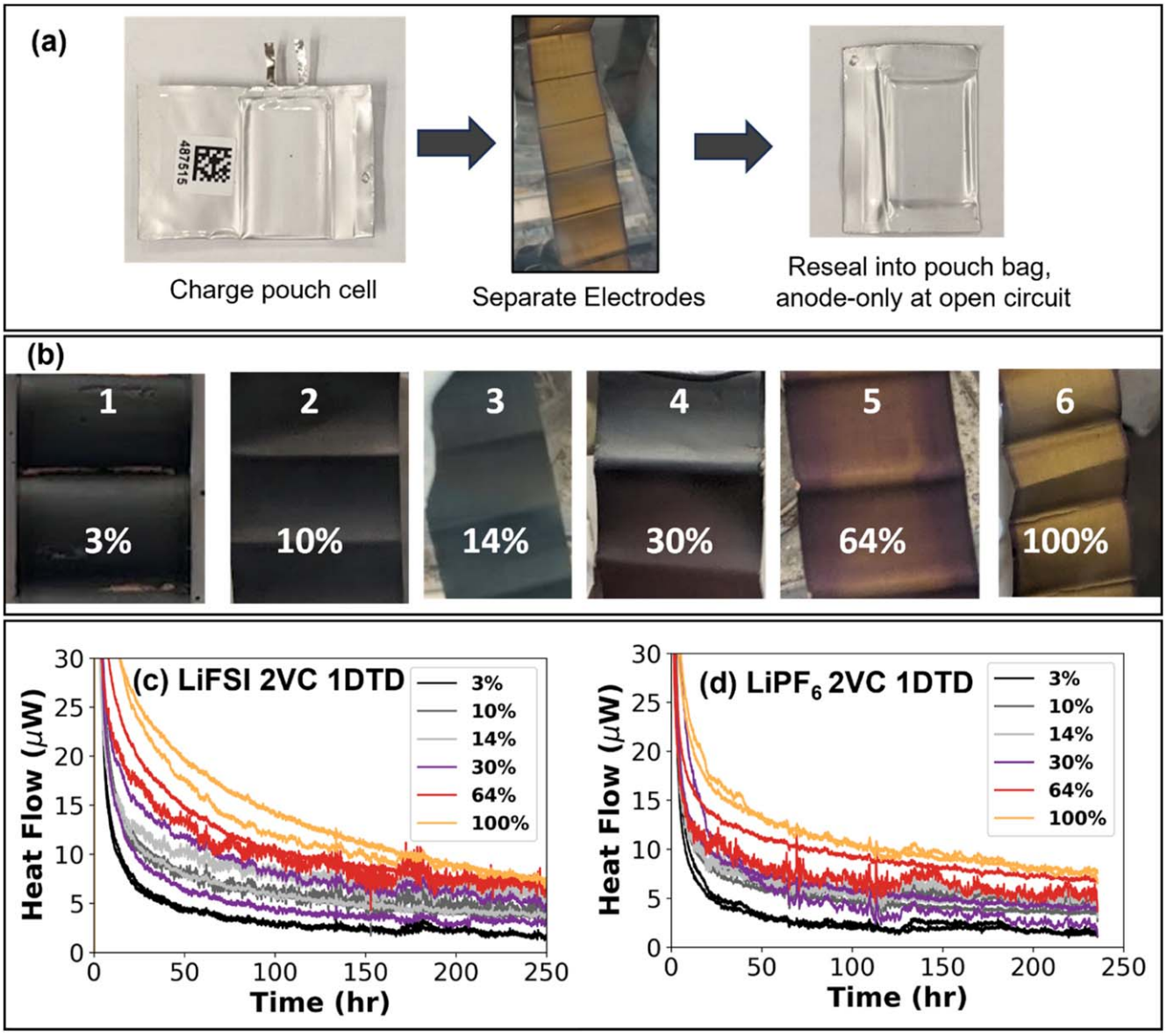

Figure 5. Isothermal microcalorimetry testing of lithiated graphite electrodes (Li_xC_6) from NMC532/AG cells after formation at 40 °C. (a) Pouch bag construction procedure from lithiated negative electrodes. (b) Photographs of the extracted graphite electrodes charged to a set of 6 known states of charge, opened in an Ar-filled glovebox, with SOC labelled on each photo. Measured parasitic heat flow vs time generated from lithiated graphite reacting with electrolyte in the open circuit pouch bags, showing decay with time, with (c) LiFSI salt and (d) $LiPF_6$ electrolyte salts. Exothermic heat flows are shown as positive.

shown to have incredible lifetime with no transition metal deposition or impedance growth, and have negative side lithium inventory loss as the only failure mechanism.[10,29] These cells have a sloping voltage curve shown in Fig. S3 compared to LFP's flat voltage profile, so we can identify the SOC more accurately. After charging to the specified voltages shown in Table S1, a voltage hold for 36 h was performed to equilibrate the cells at a constant SOC. A voltage hold longer than 36 h may be necessary for the graphite in the overhang region to become uniformly lithiated with the bulk of the cell.[30] Some repeated experiments with a 300 h voltage hold are shown in Fig. S4. A longer voltage hold creates a more uniform SOC across the electrode, and this minimizes the thermal transient, but does not affect the steady state heat flow results. The cells were disassembled in their charged states in an Argon-filled glovebox and resealed into separated electrode pouch bags, which had IMC testing done at 40 °C for >200 h.

Figure 5a shows the pouch bag construction process, Fig. 5b shows photos of the lithiated graphite electrodes at the specified states of charge, and Figs. 5c, 5d show the measured open circuit parasitic heat flows decaying with time in the calorimeter. All heat flows of lithiated graphite reacting with electrolyte decay with time as the SEI matures, and this corresponds to models[17,31,32] showing an SEI growth rate proportional to time$^{0.5}$. There is more heat flow and reactivity at higher SOC, despite the graphite electrode potential being nearly constant ~0.1 V vs Li/Li^+ throughout most of the SOC range. The faster capacity fade rate of high SOC LFP cells shown in Figs. 2–3 can be directly attributed to the elevated reactivity between lithiated graphite and electrolyte shown in Fig. 5. Figures 5c–5d shows that electrodes with LiFSI in the electrolyte produce more heat than with $LiPF_6$ initially, but after sufficient relaxation > 200 h, there is no difference between lithiated graphite reactivity in the presence of LiFSI vs $LiPF_6$, likely because electrodes in both cases are sufficiently passivated with 2% VC 1% DTD additives. The parasitic heat flow traces shown in Figs. 5c–5d would likely continue asymptotically over time until all lithium inventory in the graphite is depleted in this SEI growth process. The enthalpy for this reaction is

known to be −3 eV Li^{-1} atom,[33] for fully lithiated graphite (LiC_6). Figure S4c shows how parasitic heat flow increases with SOC, independent of graphite type or salt type. In summary, a high degree of lithiation of graphite electrodes causes more reactivity with electrolyte, measured through continuous parasitic heat flow. This mechanism shown in isolated graphite electrodes is present in LFP cells as well, and we believe this reactivity at higher SOC is responsible for elevated rates of lithium inventory loss when LFP is cycled at high average SOC.

After showing that SEI growth is exothermic and increases more rapidly at higher states of charge, we can understand how the electrolyte degrades in the LFP cells. Cycling LFP/AG cells across the 75%–100% SOC window means faster electrolyte reduction and faster consumption of the VC additive during cycling as the SEI repairs and grows over the 2500 h tested. To quantify electrolyte additive amounts and any degradation products, liquid GCMS and NMR were used. We identified DMOHC (dimethyl-2,5-dioxahexane carboxylate) as the only degradation product present in some of these LFP cells. Selected chromatograms are shown in Figs. 6a–6d from cells with 4 conditions: two salts and two SOC windows. The electrolytes from cells cycled over a higher average SOC window show more DMOHC than cells cycled over a lower average SOC window. The formation of DMOHC has been shown to be a reaction product between EC and DMC in the presence of a poorly passivated negative electrode which creates lithium alkoxides.[34,35] Therefore, the presence of DMOHC is an indication of a poor SEI, coinciding with the observed iron dissolution and poor cycle life. Figures 6e–6f show that the cells with VC remaining do not have DMOHC present in the electrolyte nor Fe deposition on the negative electrode. Once VC is close to consumption, then DMOHC production increases along with Fe dissolution and deposition. In this study, all cells were stopped for analysis after a constant time of 2500 h rather than a constant capacity fade, so we can observe how the gentler cycling conditions of 0%–25% SOC result in extra VC remaining in the electrolyte and with no DMOHC formation, while the harsher conditions of 75%–100% SOC consumed the VC and created more DMOHC. As seen in Figs. 6e–6f, these mechanisms are accelerated at higher temperature and with higher surface area graphite (AG2), where VC depletion occurs faster. The post-cycling gas volumes are shown in Fig. S5 and post cycling charge transfer resistance (R_{ct}) values from EIS are shown in Fig. S6.

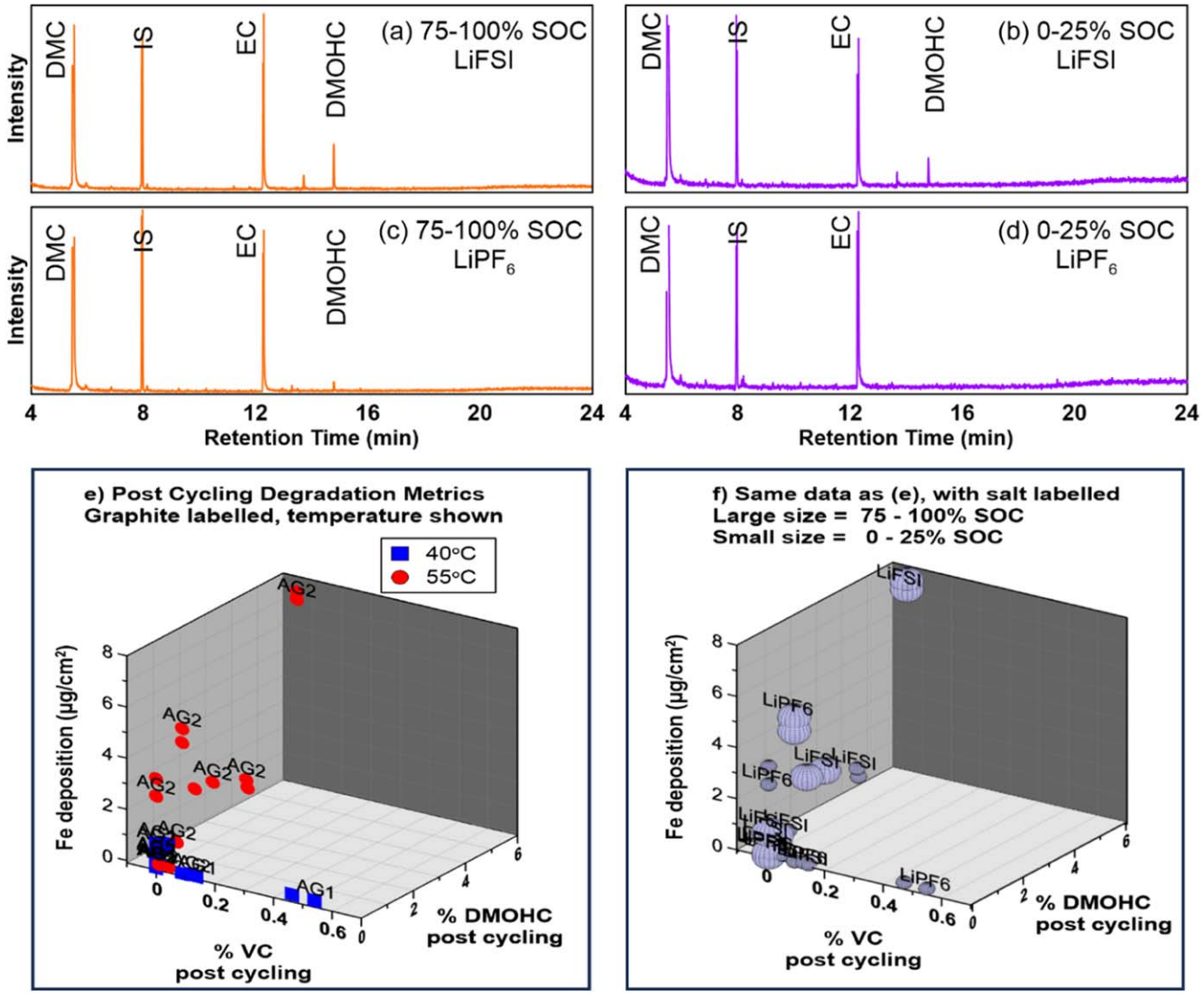

Figure 6. Electrolyte analysis results post cycling LFP/AG cells over various SOC windows for 2500 h. (a-d) Liquid GCMS chromatograms of extracted electrolyte samples after various cycling conditions from LFP/AG2 cells at 55 °C, showing solvent peaks (EC & DMC), internal standard (IS) and DMOHC as a degradation product. Chromatograms from duplicate cell extractions are exactly on top of each other. The peaks are scaled to DMC as 100% and the DMC and EC peaks are clipped. (e)–(f) Degradation mechanism correlation plots from all cells studied, using quantitative NMR and XRF analyses showing electrolyte VC content, Fe deposition on the negative electrode, and electrolyte DMOHC content. All cells started with 2% VC and 0% DMOHC when fresh.

Discussion

We propose a degradation pathway shown in Fig. 7 to explain why the LFP cells cycled across a higher average SOC fade faster than the lower SOC cells. At higher SOC, there is more exothermic heat flow produced from faster SEI growth and electrolyte reduction. This leads to VC being depleted at a faster rate in high SOC cycles. Additional factors that accelerate VC consumption are high temperature and higher surface area graphite (AG2 in this work). Once VC is consumed, then new SEI growth cannot come from VC reduction, so lithium alkoxides form from linear carbonate reduction[36] and DMOHC begins to form on the imperfectly passivated graphite.[35] At the same time, iron dissolution from the positive electrode and deposition onto the negative starts to occur. We propose that the Fe dissolution is caused by lithium alkoxides, and this chemical mechanism is verified in Fig. 8. After the Fe dissolves from LFP and transports in the electrolyte, Fe deposition onto the negative electrode is accelerated at high SOC (on lithiated graphite). New electrolyte reduction at those Fe sites on the graphite leads to more rapid capacity fade through lithium inventory loss. Therefore, cycling LFP cells over high SOC has two mechanistic reasons for accelerating failure. First it causes faster electrolyte additive consumption due to the increased reactivity of highly lithiated graphite which accelerates the production of lithium alkoxides. Second, these lithium alkoxides cause Fe dissolution and subsequent deposition on the graphite negative electrode which accelerates Li inventory loss.

It is important to note that we cannot make conclusive lifetime extrapolation statements, because these cells were stopped for destructive analysis after only 2500 h of testing. The best performing cells retained 97% capacity at that time, while the worst performing cells retained 76% capacity. Some preliminary unpublished results on smaller sample sizes suggest that LFP cells cycled at high average SOC may not experience a continuously rapid capacity fade and could recover in later cycles. More work will be done to investigate this mechanism after longer cycling times.

To test our hypothesis about whether lithium alkoxides are causing iron dissolution in LFP cells, we added lithium methoxide ($LiOCH_3$) artificially to an electrolyte. We wanted to simulate a realistic cell scenario where the graphite SEI is sufficiently passivated with 2 VC in formation without any $LiOCH_3$, and instead of waiting for $LiOCH_3$ to be produced from DMC reduction, we added an injection of 1% $LiOCH_3$ in EC:DMC 3:7 1.5 M LiFSI after formation in a second electrolyte filling step. This process is shown in Fig. 8a, with LFP/AG1 cells undergoing a formation cycle and a subsequent constant voltage hold at 2.5 V (0% SOC) or 3.65 V (100% SOC) for 36 h at 40 °C. Then 8 of the cells were disassembled into positive electrode only pouch bags and 8 cells remained as full pouch cells, including duplicates. The cells and pouch bags were stored for 10 d at 70 °C with either control or 1% $LiOCH_3$ electrolyte. Then the electrolytes were extracted for ICP analysis of dissolved Fe, and the negative electrodes were extracted for XRF of deposited Fe. Figure 8b shows that the Fe concentration in the electrolytes of positive pouch bags increases in the presence of 1% $LiOCH_3$ from 0.5 ppm to 3.0 ppm, and the SOC has minimal impact. In the full cells, the control condition already has some Fe dissolution, and this may be due to naturally produced $LiOCH_3$, from DMC reduction on the graphite during 70 °C storage, or some other mechanism of crosstalk present in full cells. This result that the LFP SOC has minimal impact on Fe solubility in electrolyte indicates that Fe^{2+} and Fe^{3+} are equally likely to dissolve from LFP, and mirrors the results shown in Fig. 4b during the 1000 h long voltage holds at 60 °C. The oxidation states of the dissolved Fe were not identified in this study, but we could speculate that Li^+ and $Fe^{2+/3+}$ ion-exchange such that $Fe(OCH_3)_x$ species could be found in the electrolyte and corresponding levels of lithium ions from solution could intercalate into the LFP for charge balance. Chemical equations for these proposed reactions are shown below. At 0% SOC, Fe^{II} could ion exchange with Li^+ according to Eq. 1.

$$y\ LiOCH_3 + Li_xFePO_4 \rightarrow \frac{y}{2}Fe(OCH_3)_2 + Li_{x+y}Fe_{1-\frac{y}{2}}PO_4 \quad [1]$$

At 100% SOC, Fe^{III} could ion exchange with Li^+ according to Eq. 2.

$$y\ LiOCH_3 + FePO_4 \rightarrow \frac{y}{3}Fe(OCH_3)_3 + Li_yFe_{1-\frac{y}{3}}PO_4 \quad [2]$$

The colours observed in the extracted electrolytes with $LiOCH_3$ seen in Fig. 8a are not from Fe dissolution, but rather from VC oligomerization and DMOHC production from EC and DMC reacting. This is shown in liquid GCMS chromatograms in Fig. S7, where all conditions with $LiOCH_3$ show complete VC consumption and DMOHC production, while the control conditions have some of the 2% VC remaining from formation and no DMOHC produced.

Figure 8c shows the deposited Fe on the negative electrodes of the full cells. The control conditions had no Fe deposition (at background detection levels), and the $LiOCH_3$ conditions had significantly more Fe deposited, particularly in the 100% SOC case. This highlights an important reason why cycling near 100%

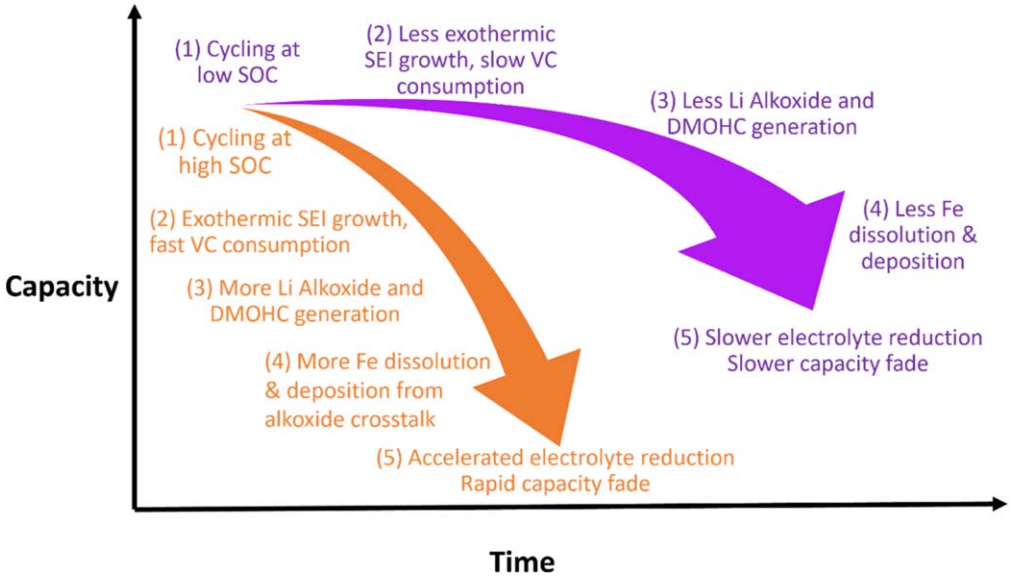

Figure 7. Proposed degradation pathways for LFP/AG cells cycling over different SOC conditions.

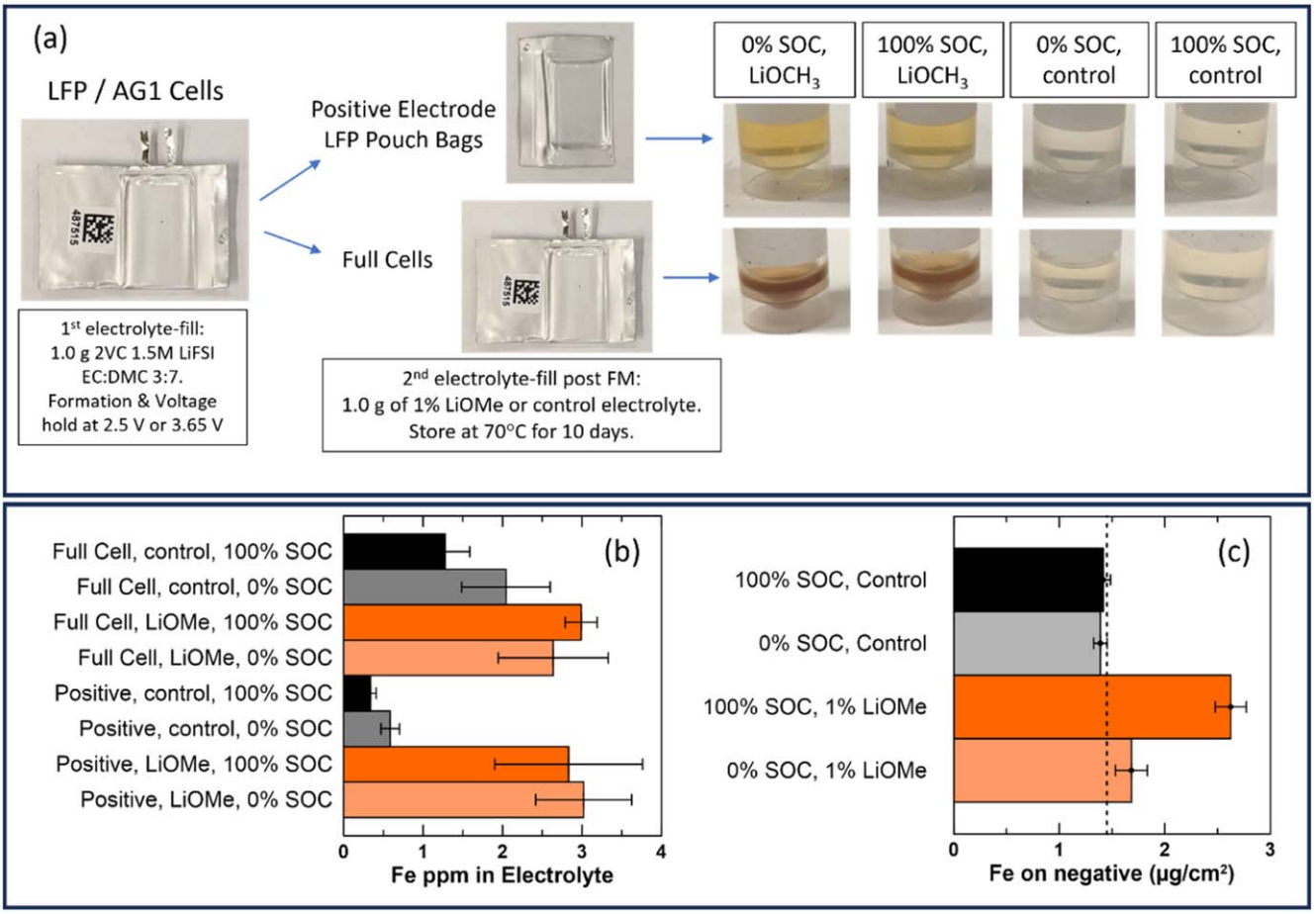

Figure 8. Lithium methoxide causing iron dissolution mechanism experiments. (a) Experimental setup with 2 electrolyte filling steps, to ensure a passivated graphite with 2 VC in formation and a subsequently injected 1% $LiOCH_3$ into full cells or positive electrode-only pouch bags. Coloured electrolytes in the $LiOCH_3$ cases are from residual VC oligomerization in solution and DMOHC production. (b) ICP results of Fe dissolved in the extracted electrolytes. (c) XRF results of Fe deposited on the negative electrodes, with dotted line showing the background Fe level.

SOC can be damaging to LFP cells: dissolved Fe is more likely to be reduced on a more reactive fully lithiated graphite with a lower potential vs Li/Li^+. These levels of Fe deposition observed after just 10 d of storage at 70 °C (1.2 µg cm^{-2}) in the presence of $LiOCH_3$ represent a significant amount of iron deposited at an accelerated rate.

Having measured the concentrations of dissolved Fe and deposited Fe in the full cells with $LiOCH_3$, we can compare the relative amounts of Fe in moles to learn whether Fe is more likely to stay dissolved in the electrolyte or to deposit on the negative electrode. The amount of Fe dissolved in the 1.0 g of electrolyte at 3.0 ppm is 5.36×10^{-8} mol, as calculated in Eq. 3.

$$n_{Fe\ electrolyte} = \frac{3.0\ \frac{\mu g}{g} \times 1.0\ g \times \frac{10^{-6} g}{\mu g}}{55.933 \frac{g}{\text{mol}}} = 5.36 \times 10^{-8}\ \text{mol} \quad [3]$$

The amount of Fe deposited on the anode is 2.13×10^{-6} mol, as calculated in Eq. 4, using a background-subtracted XRF value in the 100% SOC condition, with the geometric anode area and the Fe atomic mass.

$$n_{Fe\ anode} = \frac{1.2\ \frac{\mu g}{\text{cm}^2} \times 99.4\ \text{cm}^2 \times \frac{10^{-6} g}{\mu g}}{55.933 \frac{g}{\text{mol}}} = 2.13 \times 10^{-6} \text{mol} \quad [4]$$

Therefore, there is 40 times more Fe on the negative electrode than dissolved in the electrolyte, even though this was only 10 d of storage with $LiOCH_3$ at 70 °C. This shows that the dissolved Fe readily reduces on the charged negative electrode rather than accumulating in the electrolyte. This result verifies that our method of using XRF to identify the deposited Fe of cycled cells as a key indicator of Fe dissolution captures most of the parasitic Fe migration process. Finally, we can also estimate how much of the $LiOCH_3$ was used in the ion exchange reaction. In 1.0 g of electrolyte with 1 wt% $LiOCH_3$, there are 2.6×10^{-4} moles of $LiOCH_3$ added to the cells. Therefore, less than 1% of the added 1 wt% $LiOCH_3$ is ion-exchanged for this Fe dissolution and deposition reaction to occur. In real cells this means that extremely small concentrations of $LiOCH_3$ may exist at <0.01% in the electrolyte that could cause measurable iron dissolution.

Based on these results, we would recommend that LFP cells for long lifetime applications operate at low states of charge on average, with charging up to 100% only on occasion. This raises several questions: how practical is it to cycle a battery cell in only low SOC ranges? There is clearly a tradeoff between useful capacity and capacity retention. It is not realistic to recommend cycling LFP cells between 0%–25% SOC only, because that is a waste of capacity. However, we propose that LFP cells cycled between 0%–80% (or 0%–60%) would have a reasonable capacity and a longer lifetime than cells cycled between 0%–100%. Normalized discharge capacity retention vs time of LFP/AG1 cells cycled over these proposed fixed capacity windows are shown in Fig. 9 under (a) 40 °C and (b) 55 °C testing. These cells with different SOC windows had a constant capacity throughput during this testing time at the same current (C/3, 80 mA), but with a different number of cycles. As predicted by the

average SOC, the order of best to worst capacity retention is: 0%–25%, 0%–60%, 0%–80%, 0%–100%, 75%–100%. This data confirms that the average SOC is a determining factor in the degradation of LFP cells. These SOC window trends remain true for both salt types and both temperatures shown.

Another practical consideration is: how much does cycling LFP cells over a lower SOC window compromise the power output of that cell? For non-LFP cells, the voltage compromise may be significant, but since LFP cells have a flat voltage profile, the average discharge voltage in the 75%–100% SOC range is 3.3 V and in the 0%–25% SOC range is 3.15 V, such that there is minimal consequences to the power output when cycling at low SOC. Figure 10a shows an example voltage vs capacity profile of the LFP/AG1 pouch cells used in this work cycled with the different protocols shown including a fresh and aged check-up cycle. The aged check-up cycle shows capacity loss in the upper voltage graphite stage 2→1 plateau, indicating shift loss as reported previously to be the primary failure mode for LFP cells.[10,14] Therefore, as an LFP cell ages and the capacity fades, the average discharge voltage also decreases. The check-up cycle average discharge voltages are shown in Fig. 10b, showing that the low SOC cells stay relatively constant in voltage output, because they are not fading in capacity as significantly as the high SOC cells. Multiplying the average discharge voltage and capacity into energy output, Fig. 10c shows the energy output in the limited SOC windows and Fig. 10d shows the energy output in the check-up cycles. When cycling cells over the low SOC window, there is a slight decrease in energy output during the limited window cycles as expected due to the lower voltage. However, in the check-up cycles which represent the state of health of the cell, the low SOC cells significantly outperform the high SOC cells in energy delivered over lifetime, with a consistently high energy output after 1200 cycles. Therefore, cycling LFP cells over lower average SOC windows does not compromise on average discharge voltage nor energy output, because those cells have improved capacity retention.

Overall, this work shows that there is a trade-off between cycling LFP/graphite cells at low average SOC for improved cycling stability at the expense of a lower capacity output in the limited range cycles. Understanding this trade-off is important for EV users and grid storage operators to optimize their usage of current LFP/graphite cells. For example, in a Vehicle to Grid (V2G) scenario, electric vehicle owners could choose to operate their LFP cells between 20 to 50% SOC when they are supplying power to the grid, to maximize the cells' lifetime for their vehicle. If there is a network of vehicles connected to the grid, the lowered energy density from any given vehicle is less of a disadvantage. Therefore, this tradeoff

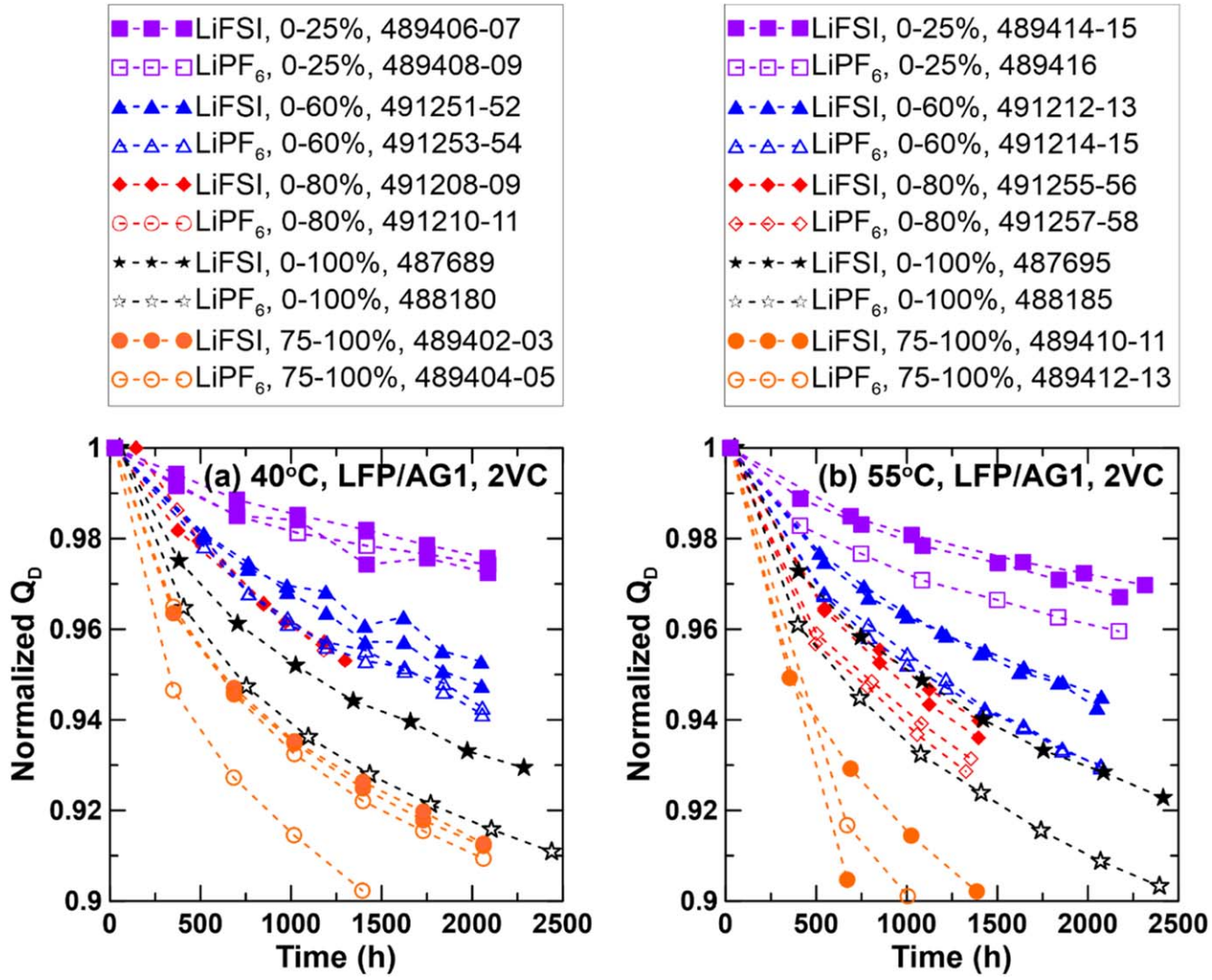

Figure 9. LFP/AG1 cell normalized discharge capacity retention cycling over 0%–60% and 0%–80% limited SOC windows, which correspond to 144 mAh and 192 mAh fixed capacity, respectively. The data from other SOC windows are from Fig. 2 for reference, shown in this same plot. The plotted cycles for all cells are the full range check-up cycles with voltage limits 2.5 V–3.65 V in (a) 40 °C and (b) 55 °C testing. All cells have 2% VC in EC:DMC 3:7 electrolyte with 1.5 M salt as indicated in the legend, alongside cell barcode IDs.

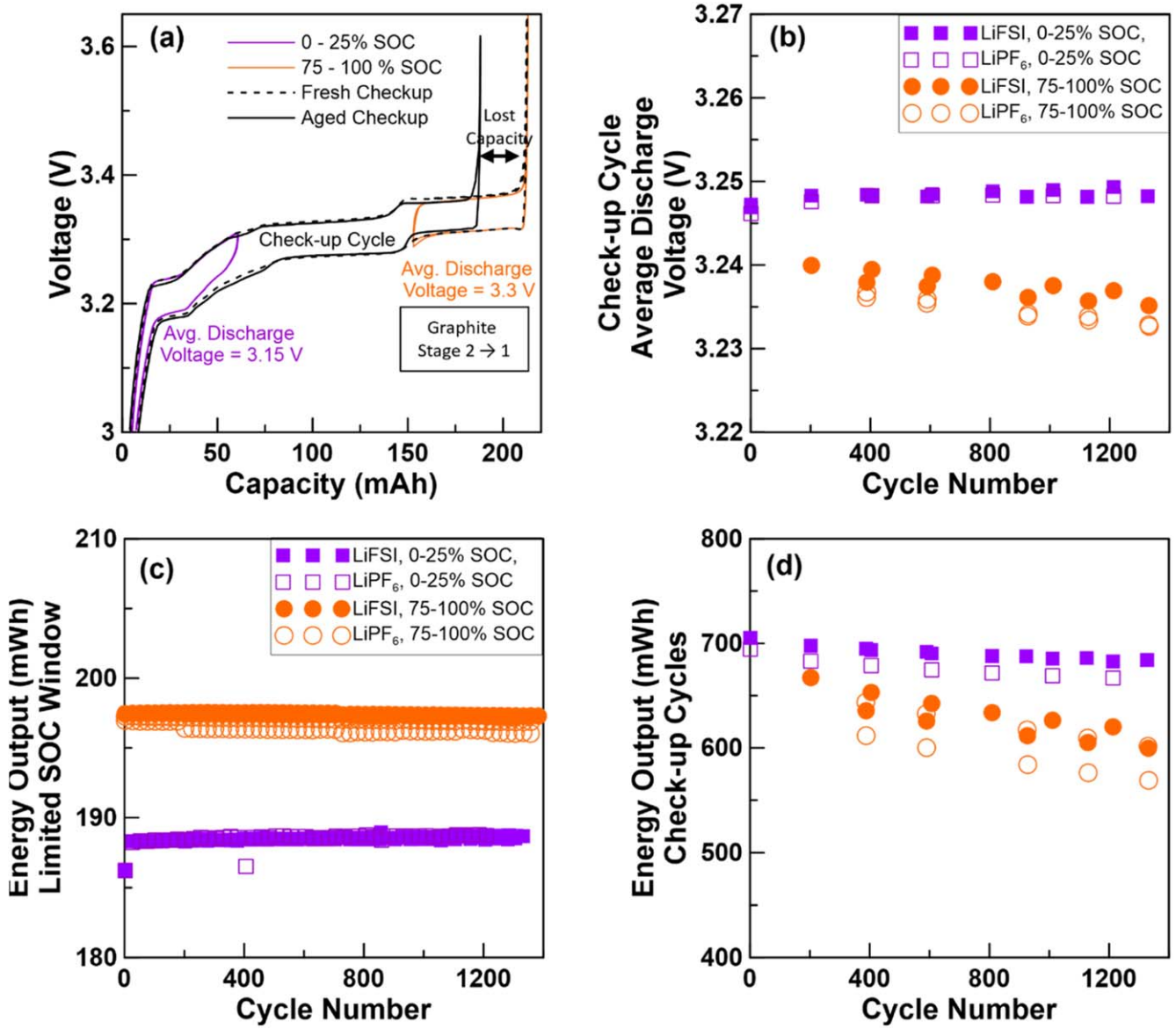

Figure 10. Energy output during cycling at various states of charge for LFP/AG1 cells at 55 °C. (a) Example voltage vs capacity curves for limited SOC windows, full checkup cycles when fresh, and aged cell checkup cycles with shift loss present. (b) Average discharge voltage vs cycle for various operation windows during the full range checkup cycles, with higher SOC showing lower voltage because of shift loss. Energy output vs cycle (c) for limited SOC window cycling and (d) for checkup cycles, showing minimal energy output differences during the 60 mAh cycling, but improvements for the lower SOC cycled cells during checkup cycles.

between energy density and lifetime is use-case dependent. The focus of this work was to show the mechanisms behind this trade-off, especially how lithium alkoxides cause Fe dissolution and how operation at high SOC increases Fe deposition and capacity fade. Future work will focus on strategies to improve LFP/graphite cells despite this trade-off, including electrolyte additives that suppress or delay lithium alkoxide generation and additives to minimize Fe dissolution. Our recommendations for other studies are to investigate LFP surface treatments, particle size, graphite type, and novel electrolyte blends as ways to mitigate cell degradation, with a focus on stabilizing the graphite SEI at high SOC.

Conclusions

Cycling near the top of charge (75%–100% SOC) is detrimental to LFP/graphite cells. Our results show a correlation between the average SOC of battery operation and capacity fade rate, meaning that the lower the average SOC, the longer the lifetime, in these 2500 h of testing. The average SOC was found to be the most critical factor influencing capacity fade for LFP cells, over the factors of temperature, depth of discharge, electrolyte salt choice or graphite choice. Cells cycled in the conventional 0%–100% SOC window showed capacity fade rates intermediate to 0%–25% and 75%–100%. Therefore, the time spent cycling at high states of charge is critical to minimize. The degradation mode of LFP/graphite cells can be summarized as lithium inventory loss from electrolyte reduction on the negative electrode, also called shift loss. Using isothermal microcalorimetry to measure parasitic heat flow from lithiated graphite pouch bags reacting with electrolyte, we show that elevated SOC causes incrementally higher reactivity. This degradation mode at high SOC most likely affects all lithium-ion cells that use a graphite negative electrode. Specific to LFP cells, iron dissolution and deposition is another degradation mode, accelerated by high temperature, imperfectly passivated negative electrodes, and time spent in high SOC cycling rather than in storage. The

chemical mechanisms for LFP/graphite cell degradation, which are accelerated at high SOC involve: (1) faster electrolyte additive depletion, (2) lithium alkoxide generation from linear carbonate reduction once VC is consumed, (3) lithium alkoxide migration to the positive electrode to cause iron dissolution by ion exchange with lithium into the LFP, (4) deposition of this iron onto the reactive lithiated graphite electrode surface, and (5) electrolyte reduction on the deposited Fe sites causing additional lithium inventory loss.

Acknowledgments

This work was funded under the auspices of the NSERC/Tesla Canada Alliance Grant program. EZ thanks the Nova Scotia Graduate Scholarship and Walter Sumner programs for scholarship support. SMA thanks the Killam Foundation and the Nova Scotia Graduate Scholarship program for scholarship support. We thank Daniel Chevalrier at the Minerals Engineering Laboratory at Dalhousie University for running the ICP-OES samples of electrolyte analysis for Fe content.

ORCID

Eniko S. Zsoldos https://orcid.org/0009-0009-5970-8154
J. R. Dahn https://orcid.org/0000-0002-6997-2436

References

1. W.-J. Zhang, "Structure and performance of LiFePO4 cathode materials: a review." *J. Power Sources*, **196**, 2962 (2011).
2. T. Feng, W. Guo, Q. Li, Z. Meng, and W. Liang, "Life cycle assessment of lithium nickel cobalt manganese oxide batteries and lithium iron phosphate batteries for electric vehicles in China." *J. Energy Storage*, **52**, 104767 (2022).
3. F. Degen, M. Winter, D. Bendig, and J. Tübke, "Energy consumption of current and future production of lithium-ion and post lithium-ion battery cells." *Nat. Energy*, **8**, 1284 (2023).
4. *Global lithium-ion battery capacity to rise five-fold by 2030*. https://woodmac.com/press-releases/global-lithium-ion-battery-capacity-to-rise-five-fold-by-2030/ (accessed 2024-01-04)Wood Mackenzie, (March 22, 2022).
5. C. P. Aiken, T. Taskovic, and J. R. Dahn, "Improved Li-Ion cell construction and usage scheme for achieving operation beyond end-of-life." *J. Electrochem. Soc.*, **169**, 090523 (2022).
6. A. K. Padhi, K. S. Nanjundaswamy, and J. B. Goodenough, "Phospho-olivines as positive-electrode materials for rechargeable lithium batteries." *J. Electrochem. Soc.*, **144**, 1188 (1997).
7. N. Ravet, S. Besner, M. Simoneau, A. Vallee, M. Armand, and J.-F. Magnan, *Electrode materials with high surface conductivity*, United States of America 6, 855, 273 B2 (Feb. 15, 2005), Patent Filed Jun. 21, 2002 https://patents.google.com/patent/US6855273B2/en.
8. L. Wang, J. Qiu, X. Wang, L. Chen, G. Cao, J. Wang, H. Zhang, and X. He, "Insights for understanding multiscale degradation of LiFePO4 Cathodes." *eScience*, **2**, 125 (2022).
9. M. Safari and C. Delacourt, "Aging of a commercial graphite/LiFePO4 cell." *J. Electrochem. Soc.*, **158**, A1123 (2011).
10. C. P. Aiken, E. R. Logan, A. Eldesoky, H. Hebecker, J. M. Oxner, J. E. Harlow, M. Metzger, and J. R. Dahn, "$Li[Ni_{0.5}Mn_{0.3}Co_{0.2}]O_2$ as a superior alternative to $LiFePO_4$ for long-lived low voltage Li-Ion cells." *J. Electrochem. Soc.*, **169**, 050512 (2022).
11. M. Kassem, J. Bernard, R. Revel, S. Pélissier, F. Duclaud, and C. Delacourt, "Calendar aging of a graphite/$LiFePO_4$ cell." *J. Power Sources*, **208**, 296 (2012).
12. Y. Zheng, Y.-B. He, K. Qian, B. Li, X. Wang, J. Li, C. Miao, and F. Kang, "Effects of state of charge on the degradation of $LiFePO_4$/graphite batteries during accelerated storage test." *J. Alloys Compd.*, **639**, 406 (2015).
13. P. Keil, S. F. Schuster, J. Wilhelm, J. Travi, A. Hauser, R. C. Karl, and A. Jossen, "Calendar aging of lithium-ion batteries: I. impact of the graphite anode on capacity fade." *J. Electrochem. Soc.*, **163**, A1872 (2016).
14. E. R. Logan, H. Hebecker, A. Eldesoky, A. Luscombe, M. B. Johnson, and J. R. Dahn, "Performance and degradation of $LiFePO_4$/graphite cells: the impact of water contamination and an evaluation of common electrolyte additives." *J. Electrochem. Soc.*, **167**, 130543 (2020).
15. E. R. Logan, A. Eldesoky, Y. Liu, M. Lei, X. Yang, H. Hebecker, A. Luscombe, M. B. Johnson, and J. R. Dahn, "The effect of $LiFePO_4$ particle size and surface area on the performance of $LiFePO_4$/graphite cells." *J. Electrochem. Soc.*, **169**, 050524 (2022).
16. E. R. Logan, A. Eldesoky, E. Eastwood, H. Hebecker, C. P. Aiken, M. Metzger, and J. R. Dahn, "The use of LiFSI and LiTFSI in $LiFePO_4$/graphite pouch cells to improve high-temperature lifetime." *J. Electrochem. Soc.*, **169**, 040560 (2022).
17. A. J. Smith, J. C. Burns, X. Zhao, D. Xiong, and J. R. Dahn, "A high precision coulometry study of the SEI growth in Li/graphite cells." *J. Electrochem. Soc.*, **158**, A447 (2011).
18. L. Von Kolzenberg, J. Stadler, J. Fath, M. Ecker, B. Horstmann, and A. Latz, "A four parameter model for the solid-electrolyte interphase to predict battery aging during operation." *J. Power Sources*, **539**, 231560 (2022).
19. A. Eldesoky, M. Bauer, S. Azam, E. Zsoldos, W. Song, R. Weber, S. Hy, M. B. Johnson, M. Metzger, and J. R. Dahn, "Impact of graphite materials on the lifetime of NMC811/graphite pouch cells: Part I. Material properties, ARC safety tests, gas generation, and room temperature cycling." *J. Electrochem. Soc.*, **168**, 110543 (2021).
20. A. Eldesoky et al., "Impact of Graphite materials on the lifetime of NMC811/graphite pouch cells: Part II. Long-term cycling, stack pressure growth, isothermal microcalorimetry, and lifetime projection." *J. Electrochem. Soc.*, **169**, 010501 (2022).
21. C. P. Aiken, J. Xia, D. Y. Wang, D. A. Stevens, S. Trussler, and J. R. Dahn, "An apparatus for the study of in situ gas evolution in Li-Ion pouch cells." *J. Electrochem. Soc.*, **161**, A1548 (2014).
22. A. S. Keefe, S. Buteau, I. G. Hill, and J. R. Dahn, "Temperature dependent EIS studies separating charge transfer impedance from contact impedance in lithium-ion symmetric cells." *J. Electrochem. Soc.*, **166**, A3272 (2019).
23. A. Eldesoky, E. R. Logan, M. B. Johnson, C. R.-M. McFarlane, and J. R. Dahn, "Scanning micro X-ray fluorescence (μXRF) as an effective tool in quantifying fe dissolution in $LiFePO_4$ cells: towards a mechanistic understanding of Fe dissolution." *J. Electrochem. Soc.*, **167**, 130539 (2020).
24. L. J. Krause, L. D. Jensen, and J. R. Dahn, "Measurement of parasitic reactions in Li Ion cells by electrochemical calorimetry." *J. Electrochem. Soc.*, **159**, A937 (2012).
25. A. J. Smith, J. C. Burns, D. Xiong, and J. R. Dahn, "Interpreting high precision coulometry results on Li-Ion cells." *J. Electrochem. Soc.*, **158**, A1136 (2011).
26. D.-I. Stroe, M. Swierczynski, A.-I. Stan, R. Teodorescu, and S. J. Andreasen, "Accelerated lifetime testing methodology for lifetime estimation of lithium-ion batteries used in augmented wind power plants." *IEEE Trans. Ind. Appl.*, **50**, 4006 (2014).
27. D.-I. Stroe, "Lifetime Models for Lithium Ion Batteries Used in Virtual Power Plants." *PhD Thesis*, Aalborg University, Denmark (2014), https://vbn.aau.dk/ws/portalfiles/portal/549543532/Lifetime_Models_for_Lithium_ion_Batteries_used_in_Virtual_Power_Plant_Applications.pdf (accessed 2024-08-05).
28. C. Delacourt and M. Safari, "Life simulation of a graphite/$LiFePO_4$ cell under cycling and storage." *J. Electrochem. Soc.*, **159**, A1283 (2012).
29. J. E. Harlow et al., "A wide range of testing results on an excellent lithium-ion cell chemistry to be used as benchmarks for new battery technologies." *J. Electrochem. Soc.*, **166**, A3031 (2019).
30. L. Streck, T. Roth, A. Noel, P. Keil, and A. Jossen, "Analysis of transient current and heat flow during voltage holds: for relaxed and unrelaxed G/NMC811 cells." *J. Electrochem. Soc.*, **171**, 070515 (2024).
31. L. Von Kolzenberg, A. Latz, and B. Horstmann, "Chemo-mechanical model of SEI growth on silicon electrode particles." *Batter. Supercaps*, **5**, e202100216 (2022).
32. L. D. Ellis, J. P. Allen, I. G. Hill, and J. R. Dahn, "High-precision coulometry studies of the impact of temperature and time on SEI formation in Li-Ion cells." *J. Electrochem. Soc.*, **165**, A1529 (2018).
33. J. Jiang and J. R. Dahn, "Dependence of the heat of reaction of $Li_{0.8}1C_6$ (0.1 V), $Li_7Ti_5O_{12}$ (1.55 V), and $Li_{0.5}VO_2$ (2.45 V) reacting with nonaqueous solvents or electrolytes on the average potential of the electrode material." *J. Electrochem. Soc.*, **153**, A310 (2006).
34. T. Taskovic, A. Adamson, A. Clarke, E. D. Alter, A. Eldesoky, K. L. Gering, K. Tuul, and J. R. Dahn, "Alkyl dicarbonates, common electrolyte degradation products, can enable long-lived Li-Ion cells at high temperatures." *J. Electrochem. Soc.*, **170**, 090527 (2023).
35. L. M. Thompson, W. Stone, A. Eldesoky, N. K. Smith, C. R.-M. McFarlane, J. S. Kim, M. B. Johnson, R. Petibon, and J. R. Dahn, "Quantifying changes to the electrolyte and negative electrode in aged NMC532/graphite lithium-ion cells." *J. Electrochem. Soc.*, **165**, A2732 (2018).
36. B. Strehle, S. Solchenbach, M. Metzger, K. U. Schwenke, and H. A. Gasteiger, "The effect of CO_2 on Alkyl carbonate trans-esterification during formation of graphite electrodes in Li-Ion batteries." *J. Electrochem. Soc.*, **164**, A2513 (2017).